Three-dimensional localization of ultracold atoms in an optical disordered potential

F. Jendrzejewski[1], A. Bernard[1], K. Müller[1], P. Cheinet[1], V. Josse[1], M. Piraud[1], L. Pezzé[1], L. Sanchez-Palencia[1], A. Aspect[1], and P. Bouyer[1,2]

Anderson localization (AL) is a quantum interference phenomenon proposed to understand how disorder can lead to the total cancelation of electron conduction. Its classical waves counterpart has been studied in acoustics, optics, and electromagnetism, but direct observation with particles remains a challenge. We report here the observation of three dimensional (3D) localization of ultracold atoms, in a disordered potential created by a speckle laser field. A phenomenological analysis of our data allows us to identify a localized component and a diffusive component. The localization we observe can be interpreted neither as classical trapping of particles with energy below the classical percolation threshold in the disorder, nor as quantum trapping in local potential minima. In contrast, our data are compatible with the self-consistent theory of AL applied to our specific situation, provided we introduce a heuristic energy shift which remains to be interpreted.

Anderson localization (AL) was proposed more than 50 years ago [1] to understand how disorder can lead to the total cancelation of electron conduction in certain materials. It is a purely quantum, one-particle effect, which can be interpreted as due to interference between the various amplitudes associated with the scattering paths of a matter wave propagating among impurities [2]. According to the celebrated scaling theory [3], AL dramatically depends on the dimension, and in the three-dimensional (3D) case, a mobility edge is predicted. It is an energy threshold separating localized states, which decay to zero at infinity and correspond to insulators, from extended states, which correspond to conductors. However, determining the precise value of the mobility edge, and the corresponding critical behavior around it, remains a challenge for microscopic theory, numerical simulations, and experiments [2]. The quest for AL has been pursued not only in condensed matter physics [4], but also in wave physics [5], and experiments have been carried out with light waves [6–9], microwaves [10,11] and acoustic waves [12]. Following theoretical proposals [13–18], recent experiments [19,20] have shown that ultracold atoms in optical disorder constitute a remarkable system to study 1D localization [21,22] or 2D diffusion [23,24] of matter waves in real space. Cold atoms in a 'kicked rotor' situation have also been used to demonstrate 1D dynamical localization [25], *i.e.*, localisation in p-space, and to study a mapping of 3D AL in that space [26]. Here, we report the observation of 3D localization of ultracold atoms of a Bose Einstein Condensate (BEC), suspended against gravity, and released in a 3D optical disordered potential with short correlation lengths in all directions. Fluorescence imaging of the expanding cloud yields density profiles composed of a steady localized part and a diffusive part. A phenomenological analysis allows us to determine the localized fraction and the diffusion coefficients of the diffusing part. The localization we observe cannot be interpreted as classical trapping of particles with energy below the classical percolation threshold in the disorder, which is well below the average energy of the atoms. Similarly, quantum trapping in local potential minima is excluded, because the local potential wells are too tight to support stationary states with energy less than the potential wells depth. In contrast, our observations are compatible with the self-consistent theory of AL [27], taking into account the specific features of the experiment, in particular the broad energy distribution of the atoms placed in the disordered potential, provided we introduce a heuristic energy shift, whose interpretation remains to be elucidated.

Experiment

Our scheme (Fig. 1a) is a generalization of the one that allowed us to demonstrate AL in 1D [15,19]. It starts with a dilute BEC with several 10^4 atoms of ^{87}Rb, initially in a shallow quasi-isotropic Gaussian optical trap (Thomas-Fermi radii of the condensate of the order of 30 μm). It is in thermal equilibrium with about the same number of uncondensed atoms. When the trap is switched off, the atoms, in the $|F = 2, m_F = -2\rangle$ hyperfine state of the ground electronic state, are kept suspended against gravity by a magnetic field gradient. The residual component of the suspending potential is isotropic and repulsive, of the form $-m\omega^2\mathbf{r}^2/2$, with $\omega \simeq 1.8$ s^{-1} (m is the atom mass). The expelling force resulting from that weak antitrapping potential is responsible for spatially inhomogeneous losses that increase with the distance to the center of the atom cloud. These losses play a role only when the expansion is large (weak or null disorder). When the expansion is small enough (strong disorder, corresponding to the points at $V_R/h \geq 400$ Hz in Figures 2-5), the inhomogeneous losses are negligible compared with observed homogeneous losses, characterized by an inverse decay time constant of ~ 0.14 s^{-1}. In the quantitative analysis, we compensate the losses by rescaling our data to a fixed total number of atoms.

In order to observe the evolution of the atomic cloud, we use a high sensitivity EMCCD camera to image, along the x-axis, the fluorescence obtained when applying for 50 μs a saturating resonant probe (Fig. 1a). This yields the column density along x, *i.e.*, $\tilde{n}(y,z,t) = \int dx\, n(x,y,z,t)$ [where $n(x,y,z,t)$ is the atomic density of the atomic cloud]. Actually, the observed 2D profile also results from a transverse averaging (perpendicular to x) due to the finite resolution of the imaging system, and to a numerical sliding average. The overall transverse resolution is 15 μm (FWHM) in the $y-z$ plane. The obtained profiles are fairly smooth, but we have performed a supplementary averaging over 3 to 5 recordings in order to increase the signal-to-noise ratio. We have not observed fluctuations correlated with a change in the realization of the disorder. This can be traced to the spatial averaging, and it is consistent with the fact that each profile is a sum of many profiles associated with different atom energy components that probe different, uncorrelated, k-components of the disordered potential. One can then consider that the observed profiles

[1]Laboratoire Charles Fabry UMR 8501, Institut d'Optique, CNRS, Univ Paris Sud 11, 2 Avenue Augustin Fresnel, 91127 Palaiseau cedex, France
[2]LP2N UMR 5298, Univ Bordeaux 1, Institut d'Optique and CNRS, 351 cours de la Libération, 33405 Talence, France.

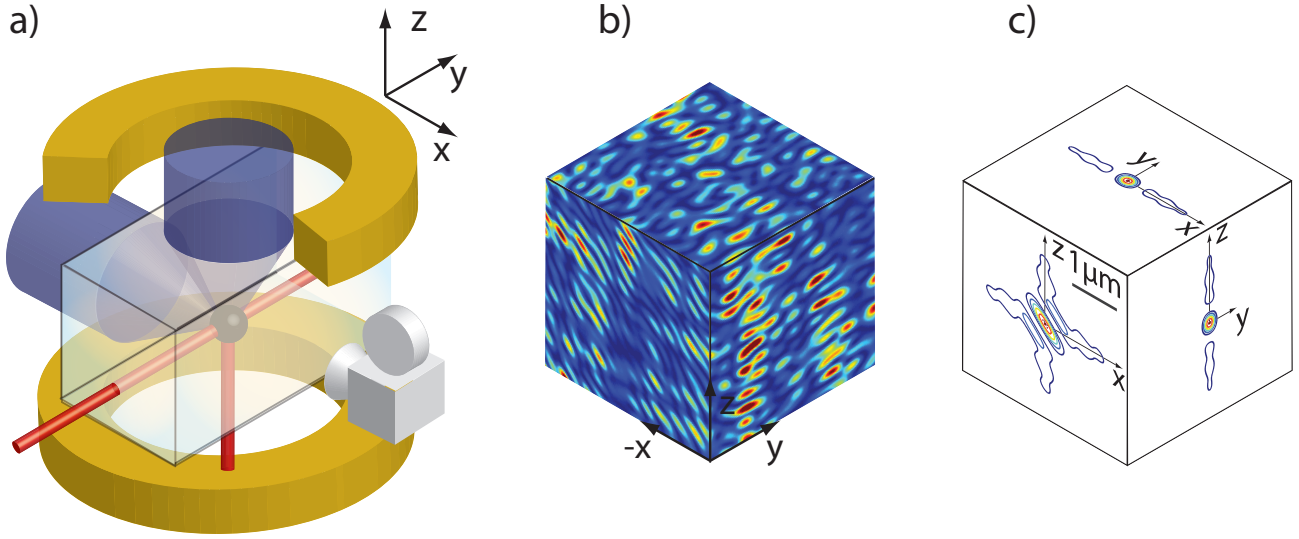

Figure 1 | **Experiment.** (a) A dilute Bose-Einstein condensate (BEC) of ultracold ^{87}Rb atoms, initially trapped by the red-detuned crossed laser beams, is released and submitted to a repulsive disordered potential. This potential is realized by the optical speckle field produced by two crossed, blue-detuned, wide coherent laser beams along the x- and z- axes, which pass through diffusive plates and are focused onto the atoms. The (paramagnetic) atoms are suspended against gravity by a magnetic field gradient (produced by the yellow coils), and the expansion of the atomic cloud can be observed for times as long as 6 s. The EMCCD camera images the fluorescence produced by a resonant probe, and yields the atomic column density integrated along the x-axis (the transverse resolution in the $y-z$ plane is 15 μm, FWHM). (b) False color representation of a realization of the disordered potential in the $x = 0$, $y = 0$, and $z = 0$ planes. (c) Plots of the 3D autocorrelation function of the disordered potential in the $x = 0$, $y = 0$, and $z = 0$ planes (the equal level lines represent levels separated by 14% of the maximum value). The correlation radii, along the main axes (axis y and the two bisecting lines of $x-z$), are 0.11 μm, 0.27 μm and 0.08 μm.

represent, within the experimental accuracy, an ensemble average over different realizations of the disorder.

We first characterize the initial atomic cloud by observing its 3D free expansion after switching off the trap, in the absence of disorder. It has two contributions: the free ballistic evolution of the condensed fraction, induced by the initial interaction energy, and the expansion of the thermal wings reflecting the velocity distribution of the initial thermal component. We then get the maximum velocity $v_{\rm max} \sim 0.5$ mm/s in the expanding BEC (corresponding to an initial chemical potential of the trapped BEC $\mu_{\rm in} = 3mv_{\rm max}^2/4$ of the order of $\mu_{\rm in}/h \simeq 40$ Hz, where h is the Planck constant). A Gaussian fit to the velocity distribution in the wings yields a rms velocity of ~ 0.3 mm/s, *i.e.*, a temperature of $T \sim 1$ nK ($k_{\rm B}T/h \sim 20$ Hz, where $k_{\rm B}$ is the Boltzmann constant).

In order to study localization, an optical disordered potential is switched on, in less than 100 μs, at time $t_{\rm i} = 50$ ms after release. At that time, the residual atom-atom interaction energy ($E_{\rm int}/h \sim 1$ Hz, estimated from the observed atomic density) has become small compared to the disorder amplitude $V_{\rm R}$ (see below). As shown in ref. 28, a well controlled disordered potential can be obtained as the intensity of the speckle field realized by passing a far detuned laser beam through a diffusive plate [29]. In order to create a 3D disorder with small correlation lengths along all directions of space, we cross two coherent orthogonal speckle fields of widths (at $\exp -2$) $\simeq 2.4$ mm (see Fig. 1a). The laser is far blue-detuned (wavelength of 532 nm, to be compared to the ^{87}Rb resonance wavelength of 780 nm), so that the disordered potential is repulsive (positive or null at any point), and spontaneous emission is negligible. The two crossed speckles have the same polarization (along the y-axis), giving an interference pattern (sketched in Fig. 1b) that yields a disordered potential $V(\mathbf{r})$ with a single-point probability distribution $\mathcal{P}(V) = V_{\rm R}^{-1}\exp(-V/V_{\rm R})$, maximum at $V = 0$. This ensures that the classical percolation threshold is small enough (less than $10^{-2}\,V_{\rm R}$) to eliminate the possibility of a classical trapping of the atoms (see Methods). This is a major advantage of using two coherent crossed speckles, rather than two speckles with orthogonal polarizations, or two incoherent speckles, for which the classical percolation threshold would be larger (the field amplitude distribution would not be Gaussian[28], and the exponential probability distribution above would not hold). The average value of the disordered potential is equal to its standard deviation $V_{\rm R}$ (named here the disorder "amplitude"), and it can be varied up to $V_{\rm R}/h = 1.1$ kHz. Figure 1c shows cuts of the autocorrelation function of the disorder. A 3D Gaussian fit of the central peak of this autocorrelation function yields standard rms radii of 0.11 μm, 0.27 μm, and 0.08 μm, along the main axes (axis y and the two bisecting lines of $x-z$), with a maximum anisotropy factor of about 3. Their geometric average provides the characteristic correlation length $\sigma_{\rm R} \simeq 0.13$ μm. The corresponding correlation energy [17] $E_{\rm R} = \hbar^2/m\sigma_{\rm R}^2$ ($E_{\rm R}/h \simeq 6.5$ kHz) is larger than the disorder amplitudes used in the experiment. We are thus in the quantum disorder regime, in which local minima of the disordered potential do not support bound states, eliminating the possibility of quantum trapping in individual local minima.

We have studied how the expansion of the released atomic cloud is affected when we apply the speckle potential with various values of the disorder amplitude $V_{\rm R}$. Figure 2a shows the evolution of the observed column density profiles for two different values of the disorder amplitude $V_{\rm R}$. For the smaller value ($V_{\rm R}/h = 135$ Hz), we observe a diffusive expansion (Fig. 2b). After 1.2 s, the density at the center has decreased enough that it is no longer observable. In contrast, for the larger value of the disorder amplitude ($V_{\rm R}/h = 680$ Hz) the diffusive expansion is slower (Fig. 2b), and an almost steady peak survives at the center for observation times as long as 6 s (Fig. 2c).

Phenomenological analysis of the data

In order to analyze these observations, we use a phenomenological model, assuming that the observed profiles are the sum of two contributions: (i) a steady localized part that is the replica of the initial profile $\tilde{n}_{\rm i}(y,z)$, *i.e.*, the BEC and its thermal wings at $t = t_{\rm i}$; (ii) a diffusive expanding part $\tilde{n}_{\rm D}(y,z,t)$, whose contribution at the center decays towards zero. More precisely, we assume that we can decompose the observed column density as

$$\tilde{n}(y,z,t) = f_{\rm loc} \times \tilde{n}_{\rm i}(y,z) + \tilde{n}_{\rm D}(y,z,t). \qquad (1)$$

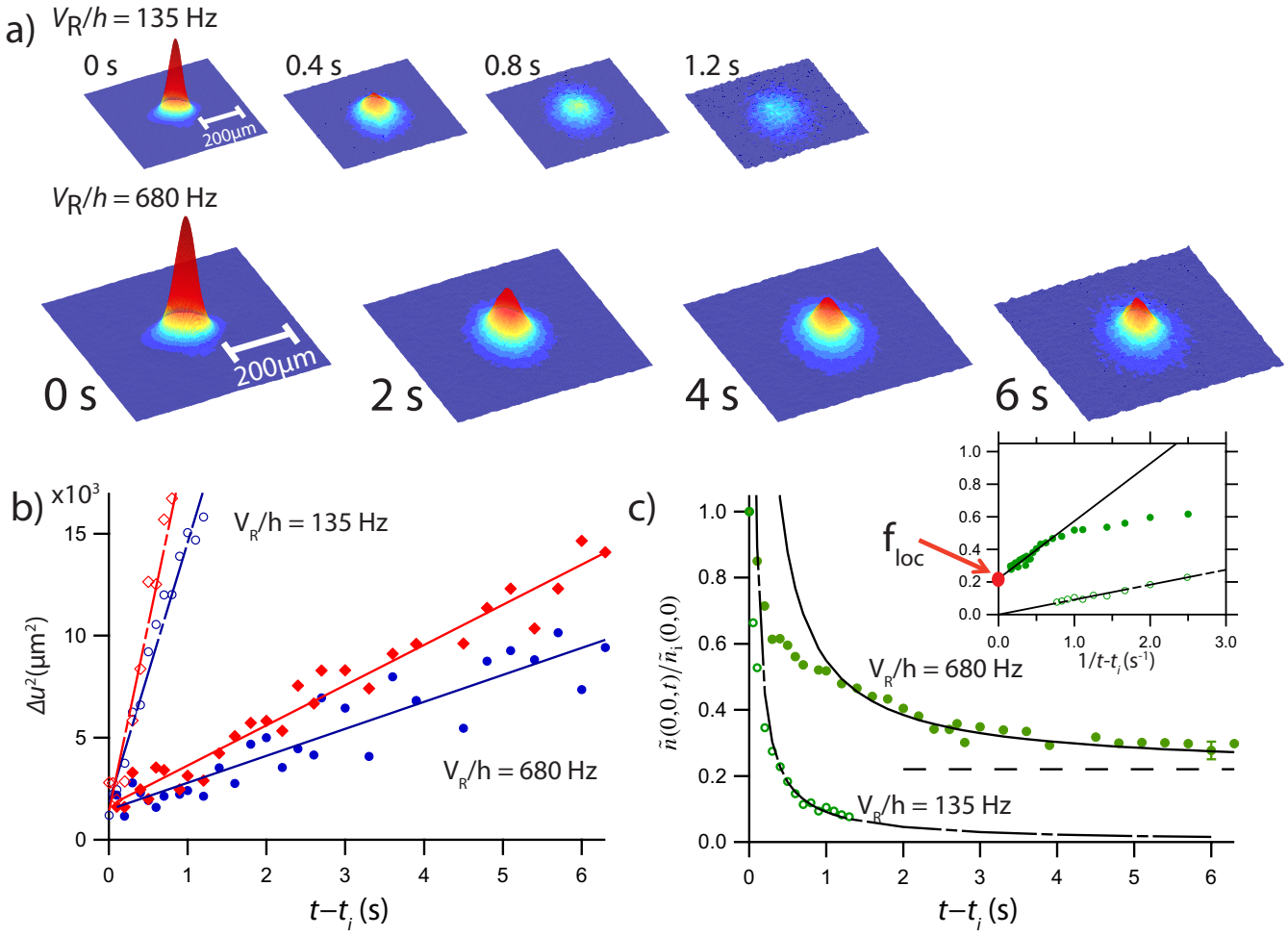

Figure 2 | Evolution of the atomic cloud for two different amplitudes of the disorder. (a) Plots of the column density in the $y-z$ plane, as observed by fluorescence imaging along the x–axis (Fig. 1a) at various delays after application of the disorder. For a weak disorder ($V_R/h = 135$ Hz), we observe an expansion leading to the disappearance of any observable atomic density for times larger than 1.2 s. For a strong disorder ($V_R/h = 680$ Hz), the atomic cloud is still well visible after 6 s, and the profile shows a steady peak around the origin, superposed on a slowly expanding component. As shown in Fig. 2b, the expanding parts have a diffusive behavior in both cases. (b) Time evolution of the mean squared widths along y (blue) and z (red) of the column density profiles, and their fits by straight lines yielding the diffusion coefficients along y and z. The anisotropy of the disorder, visible on Fig. 1b, is reflected on the diffusion coefficients. (c) Evolution of the column density at the center, and determination of its asymptotic value, yielding the localized fraction $f_{\rm loc}$ (asymptotic value of the fitted black solid line, see text).

This decomposition is supported by the observation (Fig. 2b) that the measured rms sizes Δu, along the $u \in \{y, z\}$ axes, of the column density profiles, vary as $\Delta u(t)^2 = \Delta u(t_{\rm i})^2 + 2\langle D^u\rangle(t - t_{\rm i})$. Linear fits allow us to measure the diffusion coefficients $\langle D^y\rangle$ and $\langle D^z\rangle$ (the brackets signal that we obtain mean diffusion coefficients, resulting from an average over the atoms energy distribution, see theoretical part below). Figure 2c shows that the column density at the center tends asymptotically towards a finite value, which is determined by a fit to the function $\tilde{n}(0,0,t)/\tilde{n}_{\rm i}(0,0) = A + B(t - t_{\rm i})^{-1}$, where A refers to the localized part. The $(t - t_{\rm i})^{-1}$ evolution is expected for a diffusive behavior of the column density at the center when the size of the initial profile is negligible. It results from the integration over one dimension of the $(t - t_{\rm i})^{-3/2}$ evolution expected for the 3D density at the origin. Finally, as we will see below, theory predicts that the localization lengths are smaller than the resolution of the images, so that the profile of the localized part is the replica of the initial profile, hence the form chosen for the first term in equation (1). The constant A of the fit is then interpreted as the localized fraction of atoms, $f_{\rm loc}$. It is found equal to 22% for $V_R/h = 680$ Hz, and 1% for $V_R/h = 135$ Hz. In the absence of disorder ($V_R = 0$), we fit the central density by $A + B(t - t_{\rm i})^{-2}$, as expected for a ballistic expansion, and find ($A = 0$), *i.e.*, a null localized fraction.

The phenomenological analysis of the experimental data described above has been carried out for different values of V_R. Figure 3 shows that the localized fraction, which is vanishingly small at very weak disorder, increases rapidly with V_R above $V_R/h \sim 135$ Hz, and reaches a nearly saturating value slightly larger than 20% at $V_R/h \sim 500$ Hz. Note that the inhomogeneous losses entail an overestimation of the condensed fraction for $V_R/h < 400$ Hz, so that correcting for it would result into a yet steeper increase of the observed condensed fraction. Similarly, Figure 4 shows that the measured average diffusion coefficients, $\langle D^u\rangle$, exhibit a steep decrease with the disorder amplitude V_R around the value at which a localized fraction appears, and reach almost constant values at $V_R/h \sim 500$ Hz. These values of a few $\hbar/3m$ are of the order of what is expected just above the mobility edge[17].

Theoretical description

We now compare the results of the phenomenological analysis of the experimental data with results of the theory of quantum transport and AL specifically applied to our situation, *i.e.*, taking into account: i) the spatial extension of the atomic gas at the initial time $t_{\rm i}$; ii) its energy distribution induced by the sudden application of the disordered potential at time $t_{\rm i}$; iii) the anisotropy of the 3D speckle potential. We write the

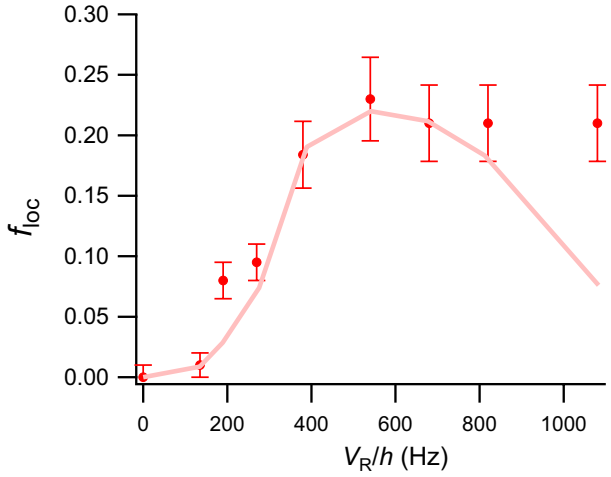

Figure 3 | Localized fraction vs. disorder amplitude. The points give the localized fraction f_{loc} determined from the decay of the central density (Fig. 2c). The error bars reflect the uncertainty on each individual fit and the fluctuations from shot to shot. For weak disorder (points with $V_R < 400$ Hz), the inhomogeneous losses, neglected in the analysis, become significant and entail an overestimation of the localized fraction. The line shows the results of the theoretical calculation, including the heuristic relative energy shift explained in the text.

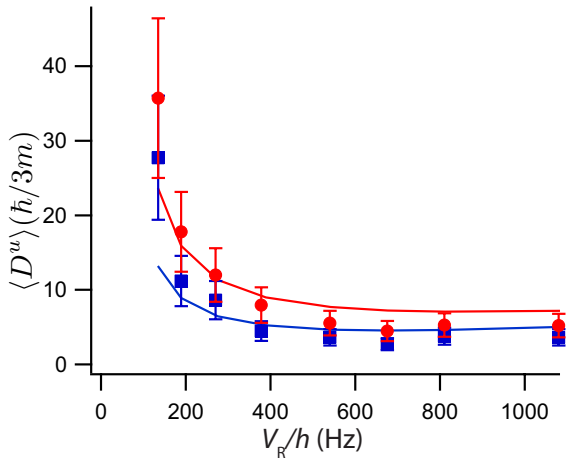

Figure 4 | Diffusion coefficient vs. disorder amplitude. The points indicate the values of the diffusion coefficients, $\langle D^u \rangle$, along the $u = y, z$ axes (blue and red points respectively), measured as explained in the text and in Fig. 2b. The error bars reflect the effect of background noise on the mean squared widths. The solid blue (y) and red (z) lines show the results of the theoretical calculation of these coefficients, using the same heuristic energy shift as in Fig. 3.

spatial density of the atomic gas as [15,16,18]

$$n(\mathbf{r},t) = \int d\mathbf{r}_i \int dE\ \mathcal{D}_i(\mathbf{r}_i,E) P(\mathbf{r}-\mathbf{r}_i, t-t_i|E)\,, \qquad (2)$$

where $\mathcal{D}_i(\mathbf{r},E)$ represents the semi-classical joint position-energy density just after the time t_i when the speckle potential is switched on, and $P(\mathbf{r}-\mathbf{r}_i, t-t_i|E)$ is the (anisotropic) probability of quantum transport, *i.e.*, the probability distribution that a particle of energy E, placed in point $\mathbf{r}_i$ at time t_i, is found in point $\mathbf{r}$ at time t.

The function $P(\mathbf{r},t|E)$, whose character changes from localized to extended when the energy passes the mobility edge E_c, plays the central role in AL. We calculate it in the framework of the self-consistent approach, within the on-shell Born approximation [27]. We use the same method as detailed in ref. 30 (except that, here, we do not include the real part of the self-energy). The incoherent (Boltzmann) diffusion tensor is first calculated using microscopic quantum transport theory, taking into account the exact correlation function of the 3D anisotropic speckle potential [31]. The terms corresponding to the quantum interference between the various diffusing paths are then incorporated in the form of the Cooperon and Hikami contributions. This provides an equation for the dynamic, quantum corrected diffusion tensor, $\mathbf{D}_*(E,\Omega)$. Solving the latter self-consistently in the long time limit (*i.e.*, the low frequency limit $\Omega \to 0$), we obtain the mobility edge E_c and the expressions of the probability of quantum transport [27,30], $P(\mathbf{r},t|E)$. Within the above approximation, we find that $E_c - V_R \simeq 1.6 V_R^2/E_R$ for our experimental parameters (*e.g.*, $[E_c - V_R]/h = 4.5$ Hz and 108 Hz for $V_R/h = 135$ Hz and 680 Hz respectively). In the AL regime ($E < E_c$),

$$P(\mathbf{r}|E) = \frac{\exp\left(-\sqrt{\mathbf{r}\cdot\mathbf{L}_{loc}^{-2}(E)\cdot\mathbf{r}}\right)}{4\pi \det\{\mathbf{L}_{loc}(E)\}\sqrt{\mathbf{r}\cdot\mathbf{L}_{loc}^{-2}(E)\cdot\mathbf{r}}} \qquad (3)$$

is a static, anisotropic, exponentially localized function, characterized by the localization tensor $\mathbf{L}_{loc}(E)$. In the diffusive regime ($E > E_c$),

$$P(\mathbf{r},t|E) = \frac{\exp\left(-\mathbf{r}\cdot\mathbf{D}_*^{-1}(E)\cdot\mathbf{r}/4t\right)}{\sqrt{(4\pi t)^3 \det\{\mathbf{D}_*(E)\}}} \qquad (4)$$

is a time-dependent, anisotropic, Gaussian function, characterized by the self-consistent diffusion tensor $\mathbf{D}_*(E)$. In the case when the range of atomic energies extends below and above the mobility edge, both expressions (3) and (4) play a role in the integral of equation (2), leading respectively to a localized component and a diffusing component.

The distribution $\mathcal{D}_i(\mathbf{r},E)$ depends on both the initial expansion of the atomic gas for $0 < t < t_i$, and the disordered potential at $t = t_i^+$. In the experiment, the sudden application of the disordered potential (in $\sim 100\mu$s) at time t_i hardly affects the density profile, $n_i(\mathbf{r})$, but significantly modifies the energy distribution since the disorder is quite strong (*e.g.*, $V_R^2/E_R \simeq \mu_{in}$ for $V_R/h \simeq 500$ Hz). For simplicity, we assume separation of the position and energy variables, *i.e.*, we write $\mathcal{D}_i(\mathbf{r},E) = n_i(\mathrm{r}) \times f_i(E)$. In order to perform the integration of equation (2), we thus need to know $n_i(\mathrm{r})$ and $f_i(E)$. The initial density profile $n_i(\mathbf{r})$ is determined from fits to the measured density profile at time t_i (see upper panels in Fig. 5). On the other hand, we do not have any simple experimental method for determining precisely the energy distribution $f_i(E)$ of the atoms in the disorder, and we calculate it from direct numerical diagonalization of the non-interacting Hamiltonian for various realizations of the disordered potential, using the sudden approximation (see Methods). We find that $f_i(E)$ is peaked around V_R (the average value of the disordered potential) with a width ΔE_{f_i} ranging from $\Delta E_{f_i}/h \sim 20$ Hz (for $V_R/h = 135$ Hz) to $\Delta E_{f_i}/h \sim 140$ Hz (for $V_R/h = 680$ Hz).

As expected, the calculation of the localized functions of equation (3) shows that the localization lengths [the components of $\mathbf{L}_{loc}(E)$] increase with the energy and diverge at the mobility edge E_c. Except in a narrow window ΔE below E_c (*e.g.*, $\Delta E/h \sim 20$ Hz for $V_R/h = 680$ Hz), however, they remain smaller than the imaging resolution (15 μm), and much smaller than the size of the atomic cloud when the disorder is switched on (Fig. 5). Since most of the energy components are outside that window, we make $P(\mathbf{r}|E) \simeq \delta(\mathbf{r})$ in equation (2) for $E < E_c$. This yields a localized profile, which is simply a replica of the initial profile $\tilde{n}_i(y,z)$ (in agreement with the first term in equation (1) used for the phenomenological analysis).

The calculated localized fraction is given by $f_{loc} = \int_{-\infty}^{E_c} dE\ f_i(E)$. When we perform this calculation, we find numerical results significantly larger than the measured values. Actually, simple inspection shows that the numerical value found for f_{loc} is extremely sensitive to numerical accuracy in the determination of $f_i(E)$ as well as to any approximation in the theoretical calculations of E_c. It is also very sensitive to uncertainties on experimental parameters, in particular the amplitude V_R and the details of the disordered potential. Considering all these uncertainties, we tried to introduce in the calculation of f_{loc} a heuristic energy shift ΔE_{heur}

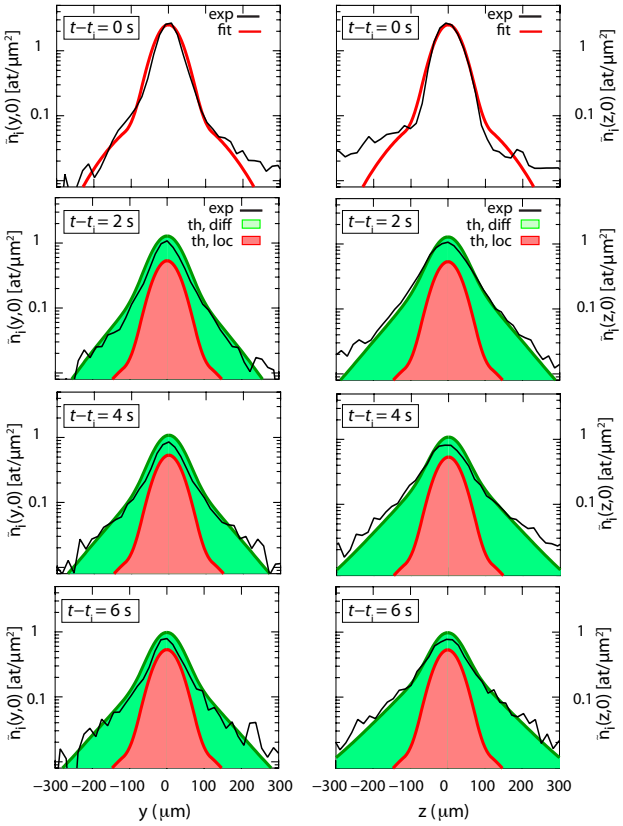

Figure 5 | Evolution of density profiles in a strong disorder ($V_R/h = 680$ Hz): experiment vs. theory. The figure shows cuts of the column density profiles along y [$\tilde{n}(y,0,t)$, left column] and z [$\tilde{n}(0,z,t)$, right column], at various delays after application of the disorder. The solid black lines are the experimental data. In the top panels (corresponding to the initial time $t = t_i$ when the disorder is switched on), the solid red lines are fits to the data. In all other panels (corresponding to $t > t_i$), the solid red lines are these fitted initial profiles multiplied by the localized fraction $f_{loc} = 0.22$, hence describing the localized part. Adding the theoretically determined diffusive parts at various delays, we obtain the green profiles, which reproduce well the experimental profiles.

between the energy functionals $f_i(E)$ and $P(\mathbf{r}|E)$, and we found that a relative shift of the form $\Delta E_{heur} = 3.35 V_R^2/E_R$ (*e.g.*, $\Delta E_{heur}/h \sim 225$ Hz for $V_R/h = 680$ Hz) leads to a fair agreement with the experimental results (see Fig. 3). Note that ΔE_{heur} is about a factor of 2 larger than $E_c - V_R$ and the width of the energy distribution ΔE_{f_i}. It thus strongly affects the value of f_{loc}.

The calculation of the diffusion coefficients involves the energy components with $E > E_c$. For consistency, we use the same energy shift as introduced in the calculation of the localized fraction, *i.e.*, we write $\langle D_*^u \rangle = \int_{E_c}^{+\infty} dE\ f_i(E - \Delta E_{heur})\ \hat{\mathbf{u}} \cdot \mathbf{D}_*(E) \cdot \hat{\mathbf{u}}$, where $\hat{\mathbf{u}}$ is the unit vector pointing along the $u \in \{y, z\}$ axis. As shown in Fig. 4, we then find a fair agreement between the results of this calculation and the experimental data. In particular, the anisotropy of the diffusion tensor is well reproduced. Note that the theoretical calculations do not involve any free parameter, apart from the heuristic energy shift discussed above.

Figure 5 shows the comparison between the theoretical and experimental profiles, at various delays, in the case of $V_R/h = 680$ Hz. In order to obtain the initial theoretical profile, we first fit the initial experimental profiles along y and z by the sum of the profiles of a BEC in the Thomas-Fermi regime and a thermal component. This allows us to calculate theoretical profiles at later times, composed of a localized part, which is a replica of the initial profile multiplied by the calculated localized fraction, plus an evolving diffusive part obtained using the calculated diffusion coefficients. The fair agreement with experimental profiles at various delays shows consistency of our theoretical analysis (including the heuristic energy shift) with the experimental observations.

This theoretical description of our experimental situation allows us to interpret the behavior of f_{loc} (Fig. 3) and $\langle D^u \rangle$ (Fig. 4) as resulting from the competition of two effects, when V_R increases. On the one hand, for each energy component, the incoherent (Boltzmann) mean free path $l_B(E)$, and thus the diffusion coefficient $D_*^u(E)$, decrease. According to the (on-shell) Ioffe-Regel criterion for localization[32], $k_E l_B(E) \lesssim 1$ (where $k_E = \sqrt{2mE}/\hbar$ is the typical particle wavevector at energy E), the mobility edge E_c then increases, so that f_{loc} increases if the atom energy distribution is unchanged. This effect dominates for weak disorder ($V_R \lesssim 400$ Hz). On the other hand, the atom energy distribution width and the heuristic shift increase with V_R, so as to populate more and more the diffusive component. The two effects counterbalance each other, and the localized fraction reaches a maximum, while the average diffusion coefficients reach almost constant values.

Conclusion

The experimental results presented here show clear evidence that when a disordered potential is applied to an expanding 3D BEC, a fraction of the atoms may get localized, while the remaining atoms have a diffusive behavior. A simple phenomenological analysis allows us to determine the localized fraction and the diffusion coefficients for various disorder amplitudes V_R, and we find that localization is observed only when the disorder is large enough. It is then natural to ask whether our observation can be interpreted as 3D AL, and whether the threshold between the two different behaviors corresponds to the mobility edge. To address the first question, we emphasize that our observations are incompatible with classical localization of particles with an energy below the classical percolation threshold, which is so small for our 3D speckle that the fraction of atoms with a lower energy is negligible. Moreover, in our situation of quantum disorder, trapping near potential minima is forbidden. We do not know then of any explanation other than AL for our observations. To go further, we have developed a theoretical model based on the self-consistent theory of AL, applied to the exact experimental situation. It allows us to calculate, for each value of the disorder amplitude, a mobility edge as well as the probability of quantum transport above and below the mobility edge. Integrating over the atom energy distribution, we obtain a good quantitative agreement with the measured localized fraction and diffusion coefficients, provided we take into account the strong modification of the atoms energy distribution when the disordered potential is applied, as calculated numerically and displaced by a heuristic shift. The calculation is however too sensitive to uncertainties in the experimental parameters, and to approximations in the theory, to permit a fully quantitative comparison. Such a comparison would be of utmost interest, the experiment being then a test-bed for theories of AL. Several future advances towards that goal can be envisaged.

On the theoretical side, it will be important to clarify the status of the heuristic energy shift. On one hand, its simple form ($\propto V_R^2$) suggests that it may be partially due to some disregarded term at Born first order, for instance the shift of energy states that is not taken into account in the on-shell approximation of the self-consistent theory of AL, but which might be significant [30,33]. On the other hand, the above form of the shift may be too simple, as suggested by the discrepancy with experimental data obtained at the highest values of V_R in Fig. 3. The search of a more elaborated form may lead to a better understanding of the localization phenomenon we have observed.

On the experimental side, it would be interesting to be able to release, in the disordered potential, a sample of atoms with a narrow energy distribution, controlled at will. It would then be possible to explore the localization transition, in particular to measure the exact value of the mobility edge E_c, and to study the critical behavior, permitting a comparison with existing theoretical treatments and hopefully suggesting routes for theoretical improvements. Beyond such developments on AL of non-interacting atoms, future experiments will include the addition of con-

trolled interactions between atoms, since the effect of interactions on AL is an open problem of major interest, in particular in 3D [4,22].

Methods

Energy distribution. When the initial chemical potential of the BEC ($\mu_{\rm in}$) and the thermal energy ($k_{\rm B}T$) are smaller than the disorder parameters, the energy distribution can be approximated by $f_{\rm i}(E) \simeq A(\mathbf{k}=0,E)$, where $A(\mathbf{k},E) = \langle \mathbf{k}|\overline{\delta(E-H)}|\mathbf{k}\rangle$ is the spectral function of the disordered medium, with $H = -\hbar^2\nabla^2/2m + V(\mathbf{r})$ the non-interacting Hamiltonian associated to a realization of the disordered potential $V(\mathbf{r})$. In order to calculate $A(\mathbf{k}=0,E)$, we decompose the operator $\delta(E-H)$ onto the energy eigenbasis, as obtained by direct numerical diagonalization of the hamiltonian H. The numerical results are obtained in a box of linear length $\sim 15\lambda$ and of grid step $\sim 0.2\lambda$ ($\lambda = 532$nm is the laser wavelength). The disorder average is performed over 100 realizations of $V(\mathbf{r})$, with the parameters of the 3D speckle potential used in the experiments.

Classical percolation and trapping in a speckle disordered potential. The percolation threshold, $E_{\rm p}$, is the energy such that all classical particles of energy $E < E_{\rm p}$ are trapped in finite-size allowed regions. We have numerically evaluated the percolation threshold of the 3D speckle potential used in the experiment (both beams with the same polarization). Using various values of the grid step, the numerical calculations provide an upper bound for the percolation threshold, $E_{\rm p} \leq 4(1)\times10^{-3}V_{\rm R}$. Note that, above $E_{\rm p}$, the fraction of classical trapping regions quickly decreases and, according to our numerical calculations, it essentially vanishes for $E \geq 8(1)\times10^{-3}\ V_{\rm R}$. Taking into account the energy distribution $f_{\rm i}(E)$ calculated numerically, with or without the heuristic energy shift (see text), we find that the fraction of classically trapped particles is negligible ($\ll 1\%$). A similar calculation with perpendicularly polarized beams yields a much higher percolation threshold $Ep \simeq 0.18(1)\ V_{\rm R}$ (note that the disordered potential probability distribution is not a decreasing exponential maximum at $V_{\rm R} = 0$, in that case).

References

1. Anderson, P. W. Absence of diffusion in certain random lattices. *Phys. Rev.* **109**, 1492–1505 (1958).
2. Lagendijk, A., van Tiggelen, B. A. & Wiersma, D. Fifty years of Anderson localization. *Phys. Today* **62**, 24–29 (2009).
3. Abrahams, E., Anderson, P. W., Licciardello, D. C. & Ramakrishnan, T. V. Scaling theory of localization: Absence of quantum diffusion in two dimensions. *Phys. Rev. Lett.* **42**, 673–676 (1979).
4. Lee, P. A. & Ramakrishnan, T. V. Disordered electronic systems. *Rev. Mod. Phys.* **57**, 287–337 (1985).
5. van Tiggelen, B. A. Localization of waves. In Fouque, J. (ed.) *Diffuse waves in complex media, Nato Advanced Science Institutes Series, Series C, Mathematical and Physical Sciences, Vol. 531*, 1 (Addison Wesley, 1999).
6. Wiersma, D. S., Bartolini, P., Lagendijk, A. & Righini, R. Localization of light in a disordered medium. *Nature* **390**, 671–673 (1997).
7. Störzer, M., Gross, P., Aegerter, C. M. & Maret, G. Observation of the critical regime near Anderson localization of light. *Phys. Rev. Lett.* **96**, 063904 (2006).
8. Schwartz, T., Bartal, G., Fishman, S. & Segev, M. Transport and Anderson localization in disordered two-dimensional photonic lattices. *Nature* **446**, 52–55 (2007).
9. Lahini, Y. *et al.* Anderson localization and nonlinearity in one-dimensional disordered photonic lattices. *Phys. Rev. Lett.* **100**, 013906 (2008).
10. Dalichaouch, R., Armstrong, J. P., Schultz, S., Platzman, P. M. & McCall, S. L. Microwave localization by 2-dimensional random scattering. *Nature* **354**, 53 – 55 (1991).
11. Chabanov, A. A., Stoytchev, M. & Genack, A. Z. Statistical signatures of photon localization. *Nature* **404**, 850–853 (2000).
12. Hu, H., Strybulevych, A., Page, J. H., Skipetrov, S. E. & van Tiggelen, B. A. Localization of ultrasound in a three-dimensional elastic network. *Nature Phys.* **4**, 845–848 (2008).
13. Damski, B., Zakrzewski, J., Santos, L., Zoller, P. & Lewenstein, M. Atomic Bose and Anderson glasses in optical lattices. *Phys. Rev. Lett.* **91**, 080403 (2003).
14. Roth, R. & Burnett, K. Phase diagram of bosonic atoms in two-color superlattices. *Phys. Rev. A* **68**, 023604 (2003).
15. Sanchez-Palencia, L. *et al.* Anderson localization of expanding Bose-Einstein condensates in random potentials. *Phys. Rev. Lett.* **98**, 210401 (2007).
16. Piraud, M., Lugan, P., Bouyer, P., Aspect, A. & Sanchez-Palencia, L. Localization of a matter wave packet in a disordered potential. *Phys. Rev. A* **83**, 031603(R) (2011).
17. Kuhn, R. C., Sigwarth, O., Miniatura, C., Delande, D. & Müller, C. A. Coherent matter wave transport in speckle potentials. *New J. Phys.* **9**, 161 (2007).
18. Skipetrov, S. E., Minguzzi, A., van Tiggelen, B. A. & Shapiro, B. Anderson localization of a Bose-Einstein condensate in a 3D random potential. *Phys. Rev. Lett.* **100**, 165301 (2008).
19. Billy, J. *et al.* Direct observation of Anderson localization of matter waves in a controlled disorder. *Nature* **453**, 891–894 (2008).
20. Roati, G. *et al.* Anderson localization of a non-interacting Bose-Einstein condensate. *Nature* **453**, 895–898 (2008).
21. Aspect, A. & Inguscio, M. Anderson localization of ultracold atoms. *Phys. Today* **62**, 30–35 (2009).
22. Sanchez-Palencia, L. & Lewenstein, M. Disordered quantum gases under control. *Nature Phys.* **6**, 87–95 (2010).
23. Robert-de-Saint-Vincent, M. *et al.* Anisotropic 2D Diffusive Expansion of Ultracold Atoms in a Disordered Potential. *Phys. Rev. Lett.* **104**, 220602 (2010).
24. Pezzé, L. *et al.* Regimes of classical transport of cold gases in a two-dimensional anisotropic disorder. *New J. Phys.* **13**, 095015 (2011).
25. Moore, F. L., Robinson, J. C., Bharucha, C., Williams, P. E. & Raizen, M. G. Observation of dynamical localization in atomic momentum transfer: A new testing ground for quantum chaos. *Phys. Rev. Lett.* **73**, 2974 – 2977 (1994).
26. Chabé, J. *et al.* Experimental observation of the Anderson metal-insulator transition with atomic matter waves. *Phys. Rev. Lett.* **101**, 255702 (2008).
27. Vollhardt, D. & Wölfle, P. Self-consistent theory of Anderson localization. In Hanke, W. & Kopalev, Y. (eds.) *Electronic Phase Transitions*, 1 (Elsevier, Berlin, 1992).
28. Clément, D. *et al.* Experimental study of the transport of coherent interacting matter-waves in a 1D random potential induced by laser speckle. *New J. Phys.* **8**, 165 (2006).
29. Goodman, J. W. *Speckle Phenomena in Optics: Theory and Applications* (Roberts and Co, Englewood, 2007).
30. Piraud, M., Pezzé, L. & Sanchez-Palencia, L. Matter wave transport and Anderson localization in anisotropic 3D disorder, arXiv:1112.2859.
31. Wölfle, P. & Bhatt, R. N. Electron localization in anisotropic systems. *Phys. Rev. B* **30**, 3542–3544 (1984).
32. Ioffe, A. F. & Regel, A. R. Non crystalline, amorphous, and liquid electronic semiconductors. *Prog. Semicond.* **4**, 237 – 291 (1960).
33. Yedjour, A. & van Tiggelen, B. A. Diffusion and localization of cold atoms in 3D optical speckle. *Eur. Phys. J. D* **59**, 249–255 (2010).
34. Kondov, S. S., McGehee, W. R., Zirbel, J. J. & DeMarco, B. Three-dimensional Anderson localization of ultracold fermionic matter. *Science* **333**, 66–68 (2011).

During the preparation of this manuscript, we have been made aware of a related work, reporting localization of fermions in a speckle potential. [34]

Acknowledgements

We thank S. Seidel and V. Volchkov for experimental contributions, M. Besbes for assistance on numerical calculations, M. Lecrivain for helping to design and realize the suspending coils, A. Villing and F. Moron for technical assistance, T. Giamarchi and B. van Tiggelen for fruitful discussions. This research was supported by the European Research Council (Starting grant "ALoGlaDis", FP7/2007-2013 Grant Agreement No. 256294, and Advanced grant "Quantatop"), the Agence Nationale de la Recherche (ANR-08-blan-0016-01), the Ministère de l'Enseignement Supérieur et de la Recherche, the Délégation Générale de l'Armement, the Triangle de la Physique and the Institut Francilien de Recherche sur les Atomes Froids. We acknowledge the use of the computing facility cluster GMPCS of the LUMAT federation (FR LUMAT 2764).

Author contributions

All authors have contributed equally.

Additional information

The authors declare that they have no competing financial interests. Correspondence and requests should be addressed to V. J. (vincent.josse@institutoptique.fr).